31. Silvestrini R, Daidone MG, Valagussa P, et al. Hydrogen-3-thymidine-labeling index as a prognostic indicator in node-positive breast cancer. *J Clin Oncol* 1990;8:1321–1326.
32. Trotter GA, Morgan GR, Goeting N, Cooper AJ, Taylor I. Prognostic factors and in vitro cytotoxic sensitivity in colorectal cancer. *Br J Surg* 1984;71:944–946.
33. Boccadoro M, Gallamini A, Fruttero A, et al. Plasma cell acid phosphatase activity as prognostic factor in multiple myeloma: relationship to the thymidine-labeling index. *J Clin Oncol* 1985;3:1503–1507.
34. Costa A, Silvestrini R, Grignolio E, Clemente C, Attili A, Testori A. Cell kinetics as a prognostic tool in patients with metastatic malignant melanoma of the skin. *Cancer* 1987;60:2797–2800.
35. Chauvel P, Courdi A, Gioanni J, Vallicioni J, Santini J, Demard F. The labelling index: a prognostic factor in head and neck carcinoma. *Radiother Oncol* 1989;14:231–237.
36. Alama A, Costantini M, Repetto L, et al. Thymidine labelling index as prognostic factor in resected non-small cell lung cancer. *Eur J Cancer* 1990;26:622–625.
37. Ohyama S, Yonemura Y, Miyazaki I. Proliferative activity and malignancy in human gastric cancers. Significance of the proliferation rate and its clinical application. *Cancer* 1992;69:314–321.
38. Meyer GJ, Schober O, Hundeshagen H. Uptake of ^{11}C-L and D-methionine in brain tumors. *Eur J Nucl Med* 1985b;10:373–376.
39. Bustany P, Chatel M, Derlon JM, et al. Brain tumor protein synthesis and histological grades: a study by PET with ^{11}C-L-Methionine. *J Neuro Oncol* 1986;3:397–404.
40. Fujiwara T, Matsuzawa T, Kubota K, et al. Relationship between histologic type of primary lung cancer and carbon-11-L-methionine uptake with positron emission tomography. *J Nucl Med* 1989;30:33–37.
41. Ogawa T, Kanno I, Shishido F, et al. Clinical value of PET with ^{18}F-fluorodeoxyglucose and L-methyl-^{11}C-methionine for diagnosis of recurrent brain tumor and radiation injury. *Acta Radiol* 1991;32:197–202.
42. Leskinen-Kallio S, Nagren K, Lehikoinen P, Ruotsalainen U, Joensuu H. Uptake of ^{11}C-methionine in breast cancer studied by PET. An association with the size of S-phase fraction. *Br J Cancer* 1991a;64:1121–1124.
43. Miyazawa H, Arai T, Iio M, Hara T. PET imaging of non-small-cell lung carcinoma with carbon-11-methionine: relationship between radioactivity uptake and flow-cytometric parameters. *J Nucl Med* 1993;34:1886–1891.
44. Bedford JS, Mitchell JB. The effect of hypoxia on the growth and radiation response of mammalian cells in culture. *Br J Radiol* 1974;47:687–696.
45. Shrieve DC, Deen DF, Harris JW. Effects of extreme hypoxia on the growth and viability of EMT6/SF mouse tumor cells in vitro. *Cancer Res* 1983;43:3521–3527.
46. Spiro IJ, Rice GC, Durand RE, Stickler R, Ling CC. Cell killing, radiosensitization and cell cycle redistribution induced by chronic hypoxia. *Int J Radiat Oncol Biol Phys* 1984;10:1275–1280.
47. Loffler M. The anti-pyrimidine effect of hypoxia and brequinar sodium (NSC 368390) is of consequence for tumor cell growth. *Biochem Pharmacol* 1992;43:2281–2287.
48. Surks MI. Effect of hypoxia on in vitro incorporation of leucine-^{14}C into rat liver protein. *Am J Physiol* 1970;218:842–844.
49. Blomstrand C. Effect of hypoxia on protein metabolism in neuron- and neuroglia cell-enriched fractions from rabbit brain. *Exp Neurol* 1970;29:175–188.
50. Albrecht J, Smialek M. Effect of hypoxia, ischemia and carbon monoxide intoxication on in vivo protein synthesis in neuron and glia cell enriched fractions from rat brain. *Acta Neuropathol* 1975;31:257–262.
51. Dische S. Radiotherapy—new fractionation schemes. *Semin Oncol* 1994;21:304–310.
52. Horsman MR, Khalil AA, Siemann DW, et al. Relationship between radiobiological hypoxia in tumors and electrode measurements of tumor oxygenation. *Int J Radiat Oncol Biol Phys* 1994;29:439–442.
53. Groshar D, McEwan AJ, Parliament MB, et al. Imaging tumor hypoxia and tumor perfusion. *J Nucl Med* 1993;34:885–888.
54. Moore RB, Chapman JD, Mercer JR, et al. Measurement of PDT-induced hypoxia in Dunning prostate tumors by iodine-123-iodoazomycin arabinoside. *J Nucl Med* 1993;34:405–411.
55. Yang DJ, Wallace S, Cherif A, et al. Development of F-18-labeled fluoroerythronitroimidazole as a PET agent for imaging tumor hypoxia. *Radiology* 1995;194:795–800.
56. Chapman JD. Measurement of tumor hypoxia by invasive and non-invasive procedures: a review of recent clinical studies. *Radiother Oncol* 1991;1:13–19.
57. Kallinowski F, Wilkerson R, Moore R, Strauss W, Vaupel P. Vascularity, perfusion rate and local tissue oxygenation of tumors derived from ras-transformed fibroblasts. *Int J Cancer* 1991;48:121–127.

Quantification of Serial Tumor Glucose Metabolism

Hsiao-Ming Wu, Carl K. Hoh, Sung-Cheng Huang, Wei-Jen Yao, Michael E. Phelps and Randall A. Hawkins
Division of Nuclear Medicine and Biophysics, Department of Molecular and Medical Pharmacology, Laboratory of Structural Biology and Molecular Medicine, UCLA School of Medicine, Los Angeles, California

We developed a method to improve the quantitative precision of FDG-PET scans in cancer patients. The total-lesion evaluation method generates a correlation coefficient (r) constrained Patlak parametric image of the lesion together with three calculated glucose metabolic indices: (a) the total-lesion metabolic index ("K_{T_tle}", ml/min/lesion); (b) the total-lesion voxel index ("V_{T_tle}", voxels/lesion); and (c) the global average metabolic index ("K_{V_tle}", ml/min/voxel). **Methods:** The glucose metabolic indices obtained from conventional region of interest (ROI) and multiplane evaluation were used as standards to evaluate the accuracy of the total-lesion evaluation method. Computer simulations and four patients with metastatic melanoma before and after chemotherapy were studied. **Results:** Computer simulations showed that the total-lesion evaluation method has improved precision (%s.d. < 0.6%) and accuracy (~10% error) compared with the conventional ROI method (%s.d. ~ 5%; ~25% error). The K_{T_tle} and V_{T_tle} indices from human FDG-PET studies using the total-lesion evaluation method showed excellent correlations with the corresponding values obtained from the conventional ROI methods and multiplane evaluation (r ~ 1.0) and CT lesion volume measurements. **Conclusion:** This method is a simple but reliable way to quantitatively monitor tumor FDG uptake. The method has several advantages over the conventional ROI method: (a) less sensitive to the ROI definition, (b) no need for image registration of serial scan data and (c) includes tumor volume changes in the global tumor metabolism.

Received Nov. 23, 1994; revision accepted Oct. 8, 1995.
For correspondence or reprints contact: Carl K. Hoh, MD, Division of Nuclear Medicine and Biophysics, Department of Molecular and Medical Pharmacology, UCLA School of Medicine, 10833 Le Conte Ave., Los Angeles, CA 90095-6948.

Key Words: FDG-PET; tumor; glucose metabolism; quantitation
J Nucl Med 1996; 37:506–513

Recent studies have established the potential of FDG-PET imaging as a tumor localization procedure. These studies produced interesting insights into the prognostic and therapeutic implications of FDG uptake in tumors (*1–6*). The conventional method to estimate the net FDG phosphorylation rate constant K (ml/min/g), proportional to the glucose metabolic rate, is accomplished by three-compartmental model fitting (*7,8*) using a nonlinear regression routine or using estimates from the Patlak graphical analysis (*9*). The nonlinear regression route or Patlak graphical analysis method (*7–9*) estimates the lesion glucose metabolic rate using a time-activity curve (TAC) generated from a region of interest (ROI) in a chosen image (single-plane-single-ROI method). Glucose metabolic rate is defined by:

$$MR = [K_1^* \cdot k_3^*/(k_2^* + k_3^*)] \cdot C_p/LC = K \cdot (C_p/LC),$$

where $K = K_1^* \cdot k_3^*/(k_2^* + k_3^*)$, K_1^* and k_2^* refer to forward and reverse capillary transport of FDG, k_3^* and k_4^* refer to phosphorylation of FDG and dephosphorylation of FDG-6-PO_4, respectively, C_p is the plasma-glucose concentration and the lumped constant is a calibration term based on the difference in transport and phosphorylation kinetics between glucose and FDG (*7,8*).

Our study in patients with metastatic melanoma showed that

TABLE 1
Lesion Glucose Metabolic Indices of Four Patients with Melanoma*

Patient† no.	Study no.	K_{nlr} (ml/min/g) mean ± % s.d.‡	K_{pat} (ml/min/g) mean ± % s.d.‡
1	1	0.007 ± 24% (n = 5)	0.007 ± 9% (n = 5)
	2	0.008 ± 11% (n = 4)	0.006 ± 17% (n = 4)
2	1	0.011 ± 53% (n = 3)	0.009 ± 41% (n = 3)
	2	0.012 ± 13% (n = 3)	0.010 ± 20% (n = 3)
3	1	0.031 ± 9% (n = 3)	0.029 ± 8% (n = 3)
	2	0.029 ± 9% (n = 3)	0.029 ± 11% (n = 3)
4	1	0.021 ± 22% (n = 4)	0.017 ± 19% (n = 4)
	2	0.021 ± 21% (n = 3)	0.015 ± 14% (n = 3)

*Patients who had PET studies before (no. 1) and after (no. 2) the therapies using the conventional single-plane-single-ROI method (nonlinear regression route and Patlak graphical analysis).

†Lesion location: Patient 1: lung; Patient 2: lung; Patient 3: lymph node; Patient 4: liver.

‡Numbers in parentheses are the total different lesion planes used to estimate metabolic indices. Also, the first and last planes covering the lesion were excluded from the calculation.

a variation (%s.d.: 9 ~ 53, Table 1) of glucose metabolic indices, K_{nlr} and K_{pat} (ml/min/g) (the K values estimated using nonlinear regression route and Patlak graphical analysis, respectively), were obtained from the same lesion using conventional single-plane-single-ROI method. The large variation may result from the heterogeneity and irregular shape of the lesion (*10,11*). Since both tumor cells and non-neoplastic elements, such as necrosis, may appear simultaneously in a lesion (*12*), the conventional single-plane-single-ROI evaluation in a localized region may not reflect the global changes within a lesion. Furthermore, if lesion orientations between two scans are different, registration of the dynamic images may be required to accurately measure K_{nlr} or K_{pat} change in a localized region. If the visualization of necrosis was affected by limited resolution of the scanner (*13*), the average K from the conventional ROI methods may be underestimated, even when small ROIs were used to minimize the partial volume effect.

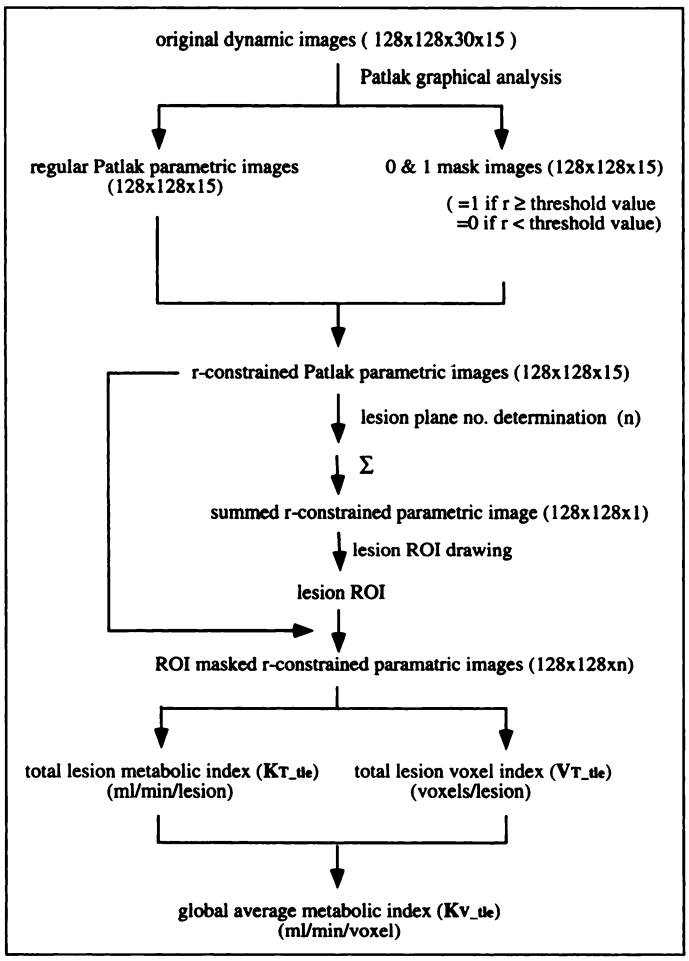

FIGURE 1. Flowchart of the total-lesion evaluation method.

In this study, we developed and tested a total-lesion evaluation method for a global assessment of tumor metabolism. The total-lesion evaluation method is based upon a parametric imaging approach that consolidates data from multiple image planes and multiple time points into a single image/numerical dataset for each lesion. The potential utility of the metabolic indices obtained from the total-lesion evaluation method was evaluated using the computer simulations and PET data from four patients with metastatic melanoma who had FDG-PET kinetic studies before and after chemotherapy. The new indices were compared to the corresponding values calculated from the conventional ROI methods (nonlinear regression route and Patlak graphical analysis) and from multiplane evaluation. In addition, these new indices were compared to the results from CT lesion volume measurements.

MATERIALS AND METHODS

Total-Lesion Evaluation

Figure 1 is a flowchart for the total-lesion evaluation method. Except for determining the image planes containing the lesion and a single ROI drawing, all subsequent steps could be automated. The total-lesion evaluation method involves:

1. Generating correlation coefficient (r) constrained Patlak parametric images (r-constrained images) from dynamic PET data by zeroing the pixel K_{pat} value if the r of the Patlak graphical analysis was below a threshold value as described by Zasadny et al. (*14*).
2. Summing up all the r-constrained images which cover the lesion.
3. Defining a single ROI which covers the whole lesion in the summed image.
4. Determining the three glucose metabolic indices: the total lesion metabolic index (K_{T_tle}, ml/min/lesion), the total lesion voxel index (V_{T_tle}, voxels/lesion) and the global average metabolic index (K_{V_tle}, ml/min/voxel).

The dynamic frames obtained from 3.5 to 40 min after FDG injection were used to generate the regular Patlak parametric images [regular K_{pat} images, pixel value: K_{pat} (ml/min/g)] using the method described by Choi et al. (*15*). Patlak graphical analysis requires a shorter scan time than the nonlinear regression route. If subject movement occurs during the study, however, the correction of movement between image frames may be necessary. The Patlak graphical analysis was evaluated on a pixel-by-pixel basis (i.e., K was estimated from pixel-by-pixel linear regression). The correlation coefficient of each linear fit was also calculated and used to generate a mask image containing 0 or 1 if r was less than or greater than a given threshold value. The r-constrained images were formed by multiplying the regular K_{pat} images with the mask images on a pixel-by-pixel, plane-by-plane basis. The image planes, which included the lesion (total plane no. = n), were summed. This summed image was used to assist in manually defining a lesion ROI large enough to contain the entire lesion. To calculate the new indices of the total-lesion evaluation method, n ROI masked r-constrained images (ROI masked r images) were

first generated from the n r-constrained images by zeroing all pixels values outside the lesion ROI. The V_{T_tle} index (voxels/lesion) was then calculated as the total voxel number where the pixel K_{pat} value in the ROI masked r images was larger than zero. The K_{T_tle} index (ml/min/lesion) was calculated by summing up all the pixel K_{pat} values of the n ROI masked r images:

$$K_{T\_tle} = \sum_{i=1}^{n} \sum_{j=1}^{N} (K_{pat_{ij}} \times Vol \times d) \qquad (N = 128 \times 128), \qquad \text{Eq. 1}$$

where $K_{pat_{ij}}$ is the K_{pat} value at pixel j of plane i, Vol is the image voxel volume and d is the inverse of the specific density of tissue and was assumed to be 1 ml/g. K_{V_tle} index (ml/min/voxel) was then calculated using Equation 2.

$$K_{V\_tle} = \frac{K_{T\_tle}}{V_{T\_tle}}. \qquad \text{Eq. 2}$$

Computer Simulations

Our simulations were intended to model the characteristics of metastases within the liver. The results also have implications for primary and metastatic tumor foci elsewhere in the body. To focus on the issue of heterogeneity due to necrotic tissue alone, we simulated a large (>2 FWHM) spherical lesion within a homogenous background. The simulated objects were 2 cm in diameter with homogeneous activity within a 4-cm background volume (128 × 128 × 128 matrix, pixel size = 0.3125 mm). A 0.5-cm central region with absence of activity was created in the center of the lesion to simulate a necrotic tumor center. This simulated object was sliced at two different axial locations (locations I and II), offset by 0.16 cm, to investigate the effects of lesion location on the conventional single-plane-single-ROI method. Four imaging planes covering the entire lesion were generated at each location (Figs. 2A, B, row 1). Each plane [128 × 128 matrix, 6.25 mm thick, which was similar to the plane thickness from a Siemens/CTI (Des Plaines, IL) 931/08 scanner (6.75 mm)] was generated by summing up twenty 128 × 128 images from the 128 × 128 × 128 simulation. The dynamic images (18 frames/plane) of two simulations (locations I and II) were generated using the simulated liver and tumor time-activity curves (TACs) (Fig. 3). The simulated TACs were generated from a three-compartment FDG model using average liver and tumor tissue rate constants obtained from a study on patients with melanoma conducted in our laboratory (unpublished data; tumor rate constants: $K_1^* = 0.243$ ml/min/g, $k_2^* = 0.780$ min^{-1}, $k_3^* = 0.101$ min^{-1}, $k_4^* = 0$ min^{-1}, normal liver rate constants: $K_1^* = 0.864$ ml/min/g, $k_2^* = 0.981$ min^{-1}, $k_3^* = 0.005$ min^{-1}, $k_4^* = 0.016$ min^{-1}). The input function was a tumor patient's plasma TAC after a bolus intravenous injection of FDG (Fig. 3). The dynamic images were then smoothed to simulate the resolution in the real PET images (FWHM ~ 9 mm). Poisson noise was added at a level typically found in human FDG studies (~7%).

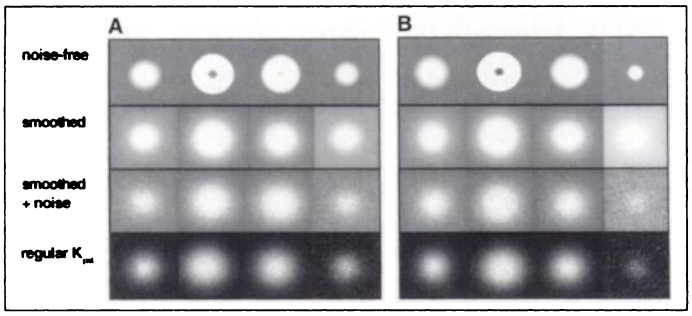

FIGURE 2. Transaxial images (left to right: plane 1-to-4) of computer simulations at (A) location 1 and (B) location 2. Row 1: no smoothing, noise-free; Row 2: smoothed only (FWHM ~ 9 mm); Row 3: smoothed and noise-added (~7%); Row 4: regular K_{pat} images from third row dynamic images.

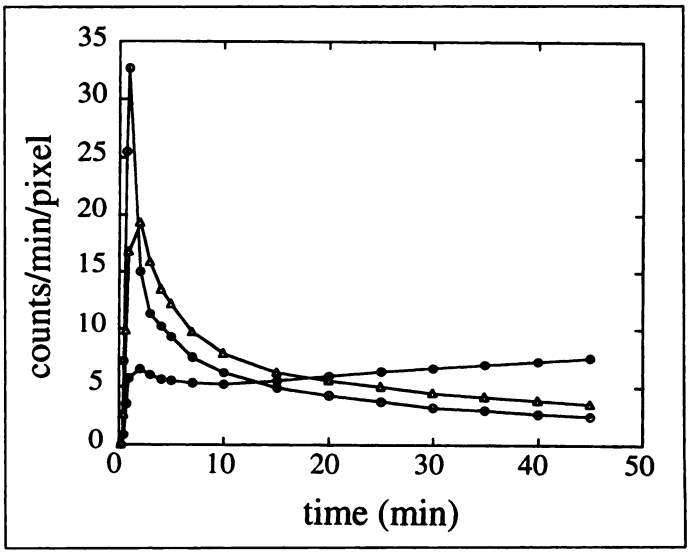

FIGURE 3. Tumor (solid circle), liver (open triangle) and plasma (open circle) TACs used in the simulation.

To evaluate the sensitivity of the total-lesion evaluation method to the r threshold value, nine heterogeneous tissue TACs were simulated, each containing 10%, 20%, 30%, 40%, 50%, 60%, 70%, 80% and 90% of tumor cells, while the remaining percentages were of normal liver metabolism based on the rate constants mentioned previously. Ten percent of plasma activity was added to each curve to simulate the vascular compartment in the tumors. Poisson noise was added to these heterogeneous TACs (~7%). The noise-free and noise-added heterogeneous TACs were then used to calculate the correlation coefficients of linear fitting using Patlak graphical analysis and determine the threshold value (r) used in the total-lesion evaluation method. All data simulations and data analysis were performed on a SPARC® 10 SUN workstation (Mountain View, CA) using a command language MATLAB® (MathWorks, Inc. Natick, MA).

Human FDG-PET studies

Twelve FDG-PET dynamic studies from four patients (Patient 1: four studies; Patient 2: three studies; Patient 3: three studies; Patient 4: two studies) with metastatic melanoma (two lung, one liver and one lymph node metastases) who had PET studies before and after chemotherapy were used. Following intravenous injection of 10 mCi of FDG, dynamic images were obtained with a Siemens/CTI 931/08 tomograph which simultaneously acquires 15 image planes 6.75 mm apart with a 10.8-cm total axial field of view. PET studies were performed at the level of the liver and spleen. The dynamic sequence consisted of twelve 10-sec, four 30-sec and fourteen 240-sec scans for a total scan time of 60 min. Cross-sectional images were reconstructed into a 128 × 128-pixel matrix using a Shepp-Logan filter with a cutoff frequency of 0.30 Nyquist frequency, yielding an in-plane spatial resolution of ~10 mm FWHM. Photon attenuation was corrected with a 20-min transmission scan using a $^{68}Ge/^{68}Ga$ external ring source. The blood samples were taken from a hand vein, heated to 44°C to arterialize the blood, at 5–10-sec intervals over the first 3 min and at progressively lengthening intervals for the remainder of the study.

Comparison of Total-Lesion Evaluation Method with Conventional ROI Method

For an accurate evaluation of the total-lesion evaluation method compared to the conventional ROI method, four analogous indices

TABLE 2
Glucose Metabolic Indices Obtained from Conventional Single-plane Single ROI (K_{pat}) and Total-Lesion Evaluation Methods (K_{T_tle})

Location	K_{pat}* (ml/min/g)	K_{T_tle}* (ml/min/lesion)	
		(r threshold = 0.6)	(r threshold = 0.7)
1	0.022 ± 0.001 (n = 6)†	0.1079 ± 0.0006 (n = 2)‡	0.1029 ± 0.0002 (n = 2)‡
2	0.021 ± 0.001 (n = 6)†	0.1081 ± 0.0004 (n = 2)‡	0.1035 ± 0.0003 (n = 2)‡
Overall	0.021 ± 0.001 (n = 12)§	0.1080 ± 0.0004 (n = 4)§	0.1032 ± 0.0004 (n = 4)§

*True values of the simulation: K_{pat} = 0.0279 ml/min/g; K_{T_tle} = 0.1150 ml/min/lesion.
†K_{pat} were estimated from three different sized ROIs in imaging planes 2 and 3 of each location (Fig. 8).
‡K_{T_tle} were calculated from two different sized ROIs in each summed r-constrained images (Fig. 8).
§Overall statistics from two locations.

("K_{T_nlr}": total lesion metabolic rate by nonlinear regression route; "K_{T_pat}": total lesion metabolic rate by Patlak graphical analysis; "K_{V_nlr}": global average metabolic rate by nonlinear regression route; "K_{V_pat}": global average metabolic rate by Patlak graphical analysis) were calculated by the nonlinear regression route and Patlak graphical analysis methods using individual ROI in multiple planes. These values were used as standards to evaluate the accuracy of the total-lesion evaluation method. The K_{T_nlr} and K_{T_pat} (ml/min/lesion) were calculated from the total K_{nlr} and K_{pat} values from n planes:

$$K_{T\_nlr} = \sum_{i=1}^{n} (K_{nlr_i} \times Vol_i \times d) \quad \text{Eq. 3}$$

$$K_{T\_pat} = \sum_{i=1}^{n} (K_{pat_i} \times Vol_i \times d), \quad \text{Eq. 4}$$

where Vol_i is the partial lesion volume (estimated from the individual ROI) in plane i, $Knlr_i$ and $Kpat_i$ are estimates from the nonlinear regression route and Patlak graphical analysis using an individual ROI in plane i, d was assumed to be 1 ml/g. In addition, the contours of n ROI masked r images from the total-lesion evaluation method were used as the reference ROIs to extract n lesion TACs. This semiautomatic ROI determination method was used to avoid operator variability in ROI drawing. K_{V_nlr} and K_{V_pat} (ml/min/voxel) were then calculated using Equations 5 and 6.

$$K_{V\_nlr} = \frac{K_{T\_nlr}}{V_{T\_tle}} \quad \text{Eq. 5}$$

$$K_{V\_pat} = \frac{K_{T\_pat}}{V_{T\_tle}}, \quad \text{Eq. 6}$$

Comparison of Total-Lesion Evaluation Method with CT Volume Measurements

The changes in K_{T_tle}, K_{V_tle}, and V_{T_tle} indices before and after therapies were compared to lesion volume changes measured from CT scans. The volume of the lesion (cm^3) was calculated as $\frac{4}{3}\pi(r_1 \times r_2 \times r_3)$, where r_1 (cm), r_2 (cm) are half of the largest length and width of the lesion in CT images, r_3 (cm) is half of the total lesion distance across the image planes. Since the entire lesion was evaluated for each study, the registration between PET and CT images was not performed.

RESULTS

Computer Simulations

Figure 2 illustrates some simulated transaxial images at two imaging planes. Noise-free unsmoothed images differed a little in appearance depending on location (row 1). The simulated necrotic core was visible. After smoothing, the simulated necrosis was difficult to identify due to the partial volume effect (row 2). With noise added, the boundaries of the lesions were even more difficult to define (row 3). The regular K_{pat} images

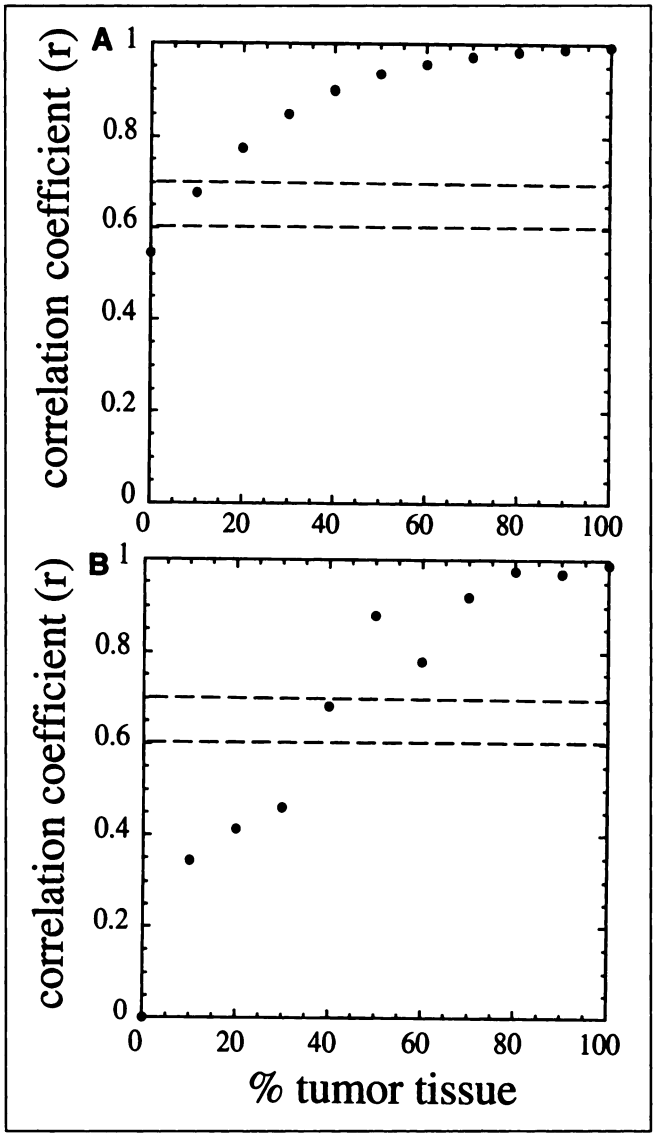

FIGURE 4. Correlation coefficients obtained from (A) noise-free and (B) noise-added (~7%) heterogeneous TACs containing different percent mass weights of tumor cells using Patlak graphical analysis. Horizontal dot lines in each plot represent the threshold values (r = 0.6 or r = 0.7) used in the total-lesion evaluation method.

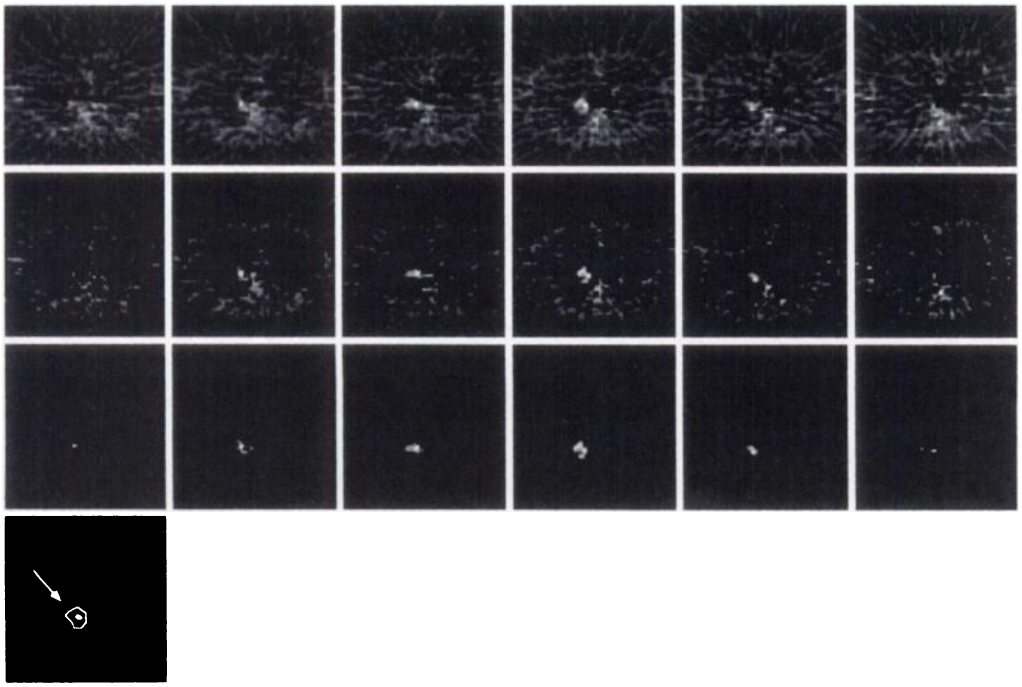

FIGURE 5. PET images of patients who had lung metastases. Row 1: regular K_{pat} (from left to right: plane 9 to 14); Row 2: r-constrained ($r \geq 0.7$); Row 3: ROI masked r-constrained; Row 4: summed r-constrained image). The ROI used in the total-lesion evaluation method was shown in the summed image.

increased the contrast between the lesion and background tissue (row 4).

Table 2 lists the results from the conventional single-plane-single-ROI method and the total-lesion evaluation method. The results show that a small variation of K_{pat} values were obtained from the same lesion if different ROI sizes and different planes were used (%s.d. ~ 5%). This variation may not be significant, since a relatively large and homogeneous lesion (>2 × FWHM) was simulated to minimize the partial volume effects (for a more realistic case, see variation of patient studies in next section). The mean value was underestimated (~75% of the true value). If, however, the total lesion metabolic index (K_{T_tle}) was used, the precision (%s.d. < 0.6%) and accuracy (~90% of the true value) of the estimates improved.

Figure 4 shows that the generation of r-constrained images was not sensitive to the r threshold values if the threshold value was within the range of 0.6 to 0.7. Within this range, only pixels, in which the percentage of tumor tissue was above a certain value (e.g., tumor tissue above 40% when ~7% of noise existed in the TAC), were included in the total lesion metabolic index calculation. Therefore, the total-lesion evaluation method minimized the background or necrotic tissue and included the majority of the tumor tissue in the calculation.

Human FDG-PET Studies

Table 1 shows the lesion glucose metabolic indices, K_{nlr} and K_{pat}, obtained from four melanoma patients who had PET studies before and after therapy using the conventional single-plane-single-ROI method. For each lesion, except for the first and last planes which cover the lesion, multiple planes were evaluated. The large standard deviations of the estimates (9 ~ 53%) demonstrated the plane dependency of the conventional ROI methods. The large variation may result from the irregular shape and heterogeneity of the lesions (metastases of Patient 1: lung; Patient 2: lung; Patient 3: lymph node; Patient 4: liver. Size of lesions are listed in Table 4). The changes of K_{nlr} and K_{pat} values between two scans were small (<15%). A good correlation of K_{nlr} and K_{pat} values from the same TACs was obtained (K_{nlr} versus K_{pat}; $y = 0.89 \times -0.0005$, $r = 0.96$, $n = 42$).

Figure 5 shows the images of one lung lesion at different planes (row 1). The ROI drawing and plane chosen in the conventional ROI method was operator-dependent. By using the total-lesion evaluation method, a single ROI was drawn on the summed r-constrained image (row 4). Due to the higher contrast in the summed image, the ROI was much easier to define. The ROI masked r-constrained images (row 3) showed that the K_{pat} values included in the calculation of the K_{T_tle} index and K_{V_tle} indices in our method were only from the lesion itself. Furthermore, these images allowed us to calculate the total voxel number, V_{T_tle}, which was related to the volume of the lesion. Figure 6 shows the correlations between K_{T_tle} and K_{T_nlr} and between K_{T_tle} and K_{T_pat} from 12 FDG-PET studies of the four melanoma patients. The correlations were close to 1.0. Similar results ($r \sim 1.0$) were obtained when K_{V_tle} was correlated with K_{V_nlr} and K_{V_pat} (Fig. 7).

Table 3 shows the K_{T_tle}, V_{T_tle}, and K_{V_tle} indices from the four patients. The K_{T_tle}, V_{T_tle} indices show that the therapies had an effect on the first patient (both values decrease more than 50%) but no effect on the other three patients (both values shows small changes or increase more that 63%). The K_{V_tle} index showed small changes in all patients (0 ~ 16%). Table 4 summarizes the index ratios of two scans using CT and PET studies. The results of CT volume measurement show that the therapies had an effect on the first patient (lesion size decrease more than 50%) but no effect on the other three patients (insignificant change or increase more than twice in lesion size).

DISCUSSION

Currently, the use of the dose uptake ratio as an index of glucose metabolism is widespread. Despite its simplicity, several studies in the literature report considerable variability when the dose uptake ratio is used (*16–18*). It was suggested by these studies that an accurate evaluation of tumor glucose metabolism should use the kinetic evaluation (*18*). Determination of the glucose metabolic rate, MR_{glc}, based on the FDG model, may be complex and time-consuming. It, however, provides a better description of tumor glycolytic characteristics. Because it incorporates the kinetics of FDG transport and phosphorylation in tissue as well as the dynamics of FDG in plasma (the input function), the total-lesion evaluation method calculates global

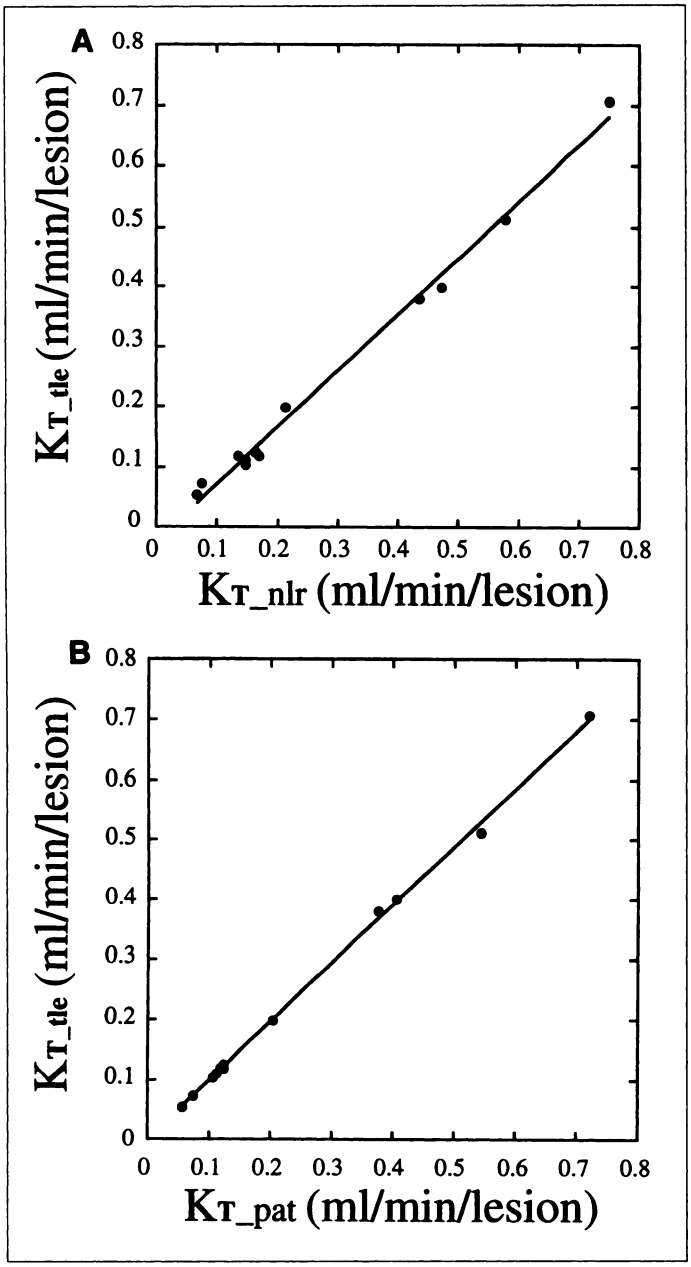

FIGURE 6. Correlations of total-lesion metabolic values using the total-lesion evaluation method and conventional methods with multiplane evaluation: (A) K_{T_tle} versus K_{T_nlr} ($y = 0.932 \times -0.019$, $r = 0.997$, $n = 12$); (B) K_{T_tle} versus K_{T_pat} ($y = 0.971 \times +0.002$, $r = 0.999$, $n = 12$).

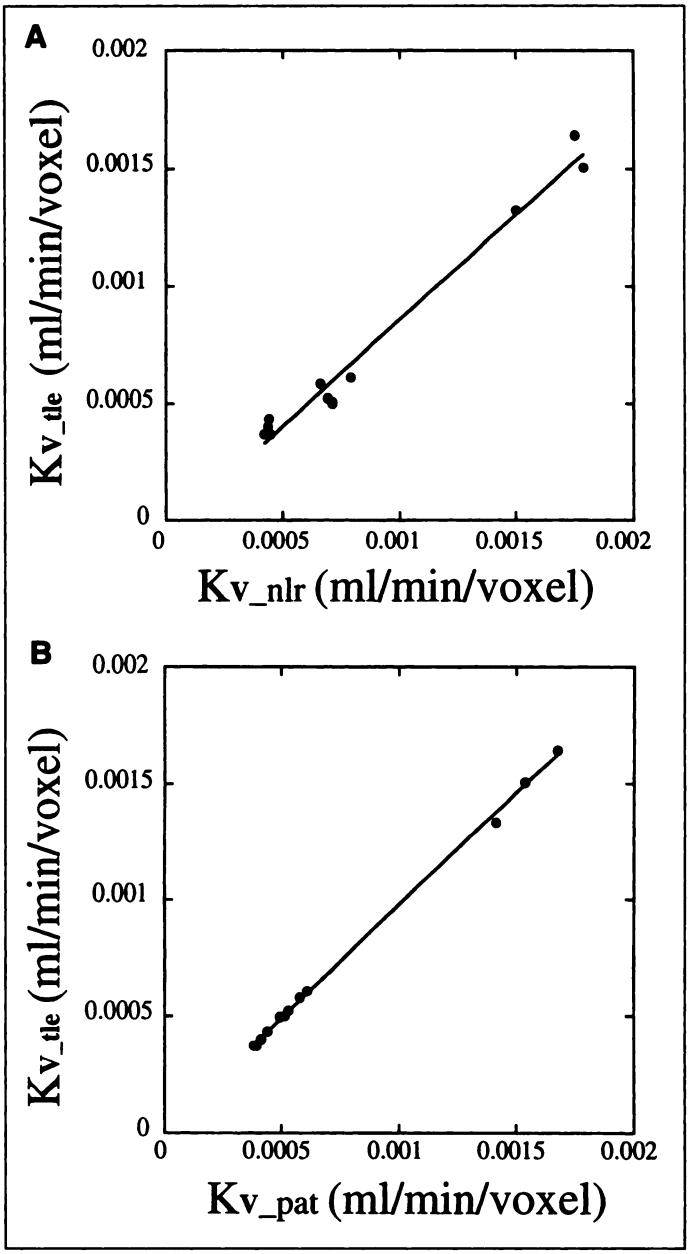

FIGURE 7. Correlations of global average metabolic values using the total-lesion evaluation method and conventional methods with multiplane evaluation: (A) K_{V_tle} versus K_{V_nlr} ($y = 0.91 \times -5.5e-5$, $r = 0.99$, $n = 12$); (B) K_{V_tle} versus K_{V_pat} ($y = 0.96 \times -8.4e-6$, $r = 1.0$, $n = 12$).

metabolic rate changes based on the FDG model and monitors the therapeutic response.

The total-lesion evaluation method was developed based on two studies. In a previous study in patients with metastatic melanoma, we found a good correlation between K_{pat} and K_{nlr}, which is consistent with the low values of k_4 in the lesions and supports the use of Patlak parametric images to quantitate glucose metabolism in the lesions (*3*). The method is computationally practical, amplifies the contrast of metastases compared with normal liver and facilitates quantification of tumor metabolism in serial imaging studies. Good correlation ($r = 0.96$, $n = 42$) of K_{pat} and K_{nlr} values obtained from four patients with metastatic melanoma lesions in liver, lung and lymph node implies the generality of the method to other organ systems. The total-lesion evaluation method adapts the r-constrained parametric imaging that has been studied by Zasadny et al. (*14*). They showed that the r-constraint improved parametric image

TABLE 3
K_{T_tle}, V_{T_tle} and K_{V_tle} Indices of Four Patients with Melanoma*

Patient no.	Study no.	V_{T_tle} (voxels/lesion)	K_{T_tle} (ml/min/lesion)	$K_{V\_tle} \times 10^{-3}$ (ml/min/voxel)
1	1	319	0.118	0.370
	2	146	0.054	0.370
2	1	211	0.111	0.522
	2	205	0.125	0.608
3	1	264	0.399	1.510
	2	429	0.706	1.646
4	1	133	0.119	0.895
	2	368	0.379	1.030

*All patients who had PET studies before (no. 1) and after (no. 2) the therapies.

TABLE 4
Ratio of Results from CT Measurements and PET Studies*

Patient no.	CT†	PET‡		
	Vol_2/Vol_1	$V_{T\_tle_2}/V_{T\_tle_1}$	$K_{T\_tle_2}/K_{T\_tle_1}$	$K_{V\_tle_2}/K_{V\_tle_2}$
1	0.52	0.46	0.46	1.00
2	0.96	0.97	1.13	1.16
3	2.58	1.63	1.77	1.09
4	4.31	2.77	3.18	1.15

*Four melanoma patients who had CT and PET studies before (subscription 1) and after (subscription 2) therapies.

†Lesion volume (Patient 1: 16.5 and 8.6; Patient 2: 1.9 and 1.8; Patient 3: 3.0 and 7.8; Patient 4: 0.69 and 2.98 cm^3, before and after therapy, respectively). Time period between two scans: Patient 1: ~2 mo; Patient 2: ~4 wk; Patient 3: ~4.5 wk; Patient 4: ~3 wk.

‡Time period between two PET studies: Patient 1 (scans 1 and 4): 23 days; Patient 2 (scans 1 and 3): 18 days; Patient 3 (scans 1 and 3): 23 days; Patient 4 (scans 1 and 2): 21 days.

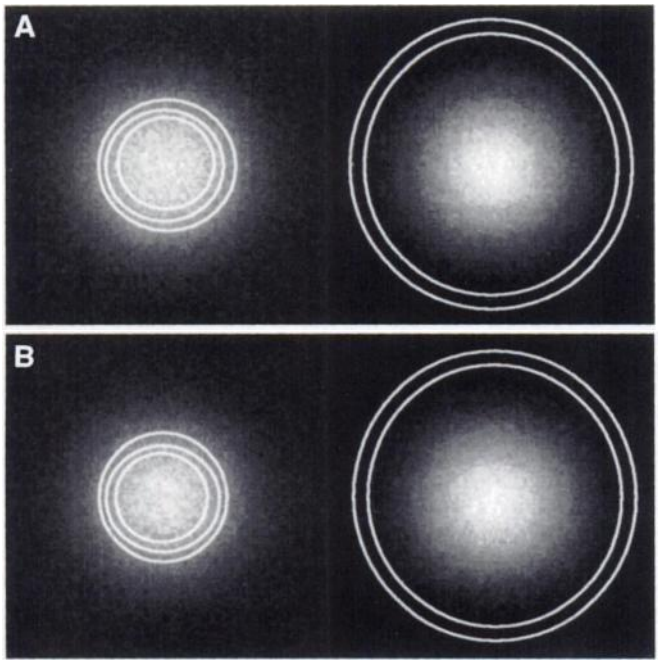

FIGURE 8. ROIs and simulated images [(upper): location 1; (bottom): location 2] used in the single-plane-single-ROI method and total-lesion evaluation method. (A) Three ROIs were used in each regular K_{pat} images (planes 2 and 3, only plane 2 images are shown). (B) Two ROIs, which are large enough to cover the whole lesion, were used in each summed r-constrained images.

quality by eliminating streak artifacts and stray pixel values that happen to produce high slope (K_{pat}) values. In addition, due to a relatively high k_4 value in normal liver tissue, the r-constrained image underestimates normal liver metabolism. Therefore, the background K_{pat} values included in the calculation of the metabolic indices in the total-lesion evaluation method can be minimized (row 3 of Fig. 5 and Fig. 8B).

The results in Table 2 show that the K_{T_tle} index was less sensitive to the ROI sizes and the threshold values as long as the ROI size was large enough to cover the whole lesion. With a lesion size exceeding what was used in the simulation, a better result was expected (due to a smaller partial volume effect when object size is much larger than 2 FWHM). Therefore, if the entire lesion is within the field of view, the registration between two dynamic studies is not necessary. Furthermore, the estimation was much closer to the true value when compared to the conventional single-plane-single-ROI method (Table 2). The V_{T_tle} index may be affected by the partial volume effect and the threshold values. With a fix threshold value, this volume index provided a good index to monitor the volume change of the lesion over time. The changes of V_{T_tle} between two PET scans of four melanoma patients showed similar results as those obtained from the CT measurements (Table 4). When the total-lesion evaluation method was compared to the conventional ROI method and multiplane evaluation, the correlation of the two methods was excellent and closed to 1.0 (Figs. 6, 7).

The ultimate goal of a FDG-PET study is to quantitate tumor glucose metabolism and predict therapeutic response. By using the K_{T_tle} and V_{T_tle} indices, the total-lesion evaluation method provides a new method to monitor the effect of therapy in cancer patients (Tables 3, 4). Whether an area or global assessment of tumor metabolism is ideal for monitoring the tumor growth may depend on the nature of the tumor type. For example, it is conceivable that areas of a tumor resistant to therapy may have focal regions of high metabolic rates while the overall tumor metabolic rate may be declining. The combined use of the conventional ROI methods on local areas and the total-lesion evaluation method may provide more insight into the biology of tumor response or nonresponse relative to glucose metabolism. In this study, melanoma metastases in different organs (lung, lymph node and liver), different shapes (spherical or irregular) and different sizes (0.69 ~ 16.5 cm^3 (Table 4) were used. Since the total-lesion evaluation method can use a larger ROI than the true lesion size (by which the recovery coefficient is calculated), the partial volume effect in the TLE method can be minimized (Table 2). Therefore, with high tumor uptake and low background activity, the TLE method may include most of the activity of a small lesion (e.g., study 2 of Patient 4, Table 3) in the calculation. When lesion size is small and with low FDG uptake, however, accurate glucose metabolic rates may not be obtainable with the total-lesion evaluation method due to limited scanner resolution. The threshold value may also affect the estimates by removing the pixel K_{pat} values in the r-constrained image when heterogeneous tissue activity is within the pixel (e.g., small percentage of tumor tissue). This may explain the underestimation of the K_{T_tle} value in the computer simulations (Table 2). Since the total-lesion evaluation method was developed to monitor the glucose metabolic change of the same lesion over time, as long as the volume change is not dramatic, the partial volume effects in serial scans should have similar effects when the total-lesion evaluation method is used. When substantial changes in tumor volume occur, however, the partial volume effects need to be taken into account.

CONCLUSION

A simple but reliable method to quantitatively monitor the total-lesion glucose metabolic changes during tumor growth is presented. Moreover, results from this method correlate with those from conventional ROI methods.

ACKNOWLEDGMENTS

The authors thank the UCLA cyclotron staff for synthesizing the FDG compound used in this study; Mr. Ron Sumida and the UCLA PET scanner staff for performing the PET studies; and Drs. E.J. Hoffman, M. Dahlbom, A.R. Ricci, K. Gardner and D. Truong for instrumentation, computer hardware and software support. This work was partly supported by Department of Energy contract DE-FC03-87ER60615 and National Institutes of Health grant RO1CA56655.

REFERENCES

1. Okazumi S, Isono K, Enomoto K, et al. Evaluation of liver tumors using fluorine-18-fluorodeoxyglucose PET: characterization of tumor and assessment of effect of treatment. *J Nucl Med* 1992;33:333–339.
2. Okada J, Yoshikawa K, Itami M, et al. Positron emission tomography using fluorine-18-fluorodeoxyglucose in malignant lymphoma: a comparison with proliferate activity. *J Nucl Med* 1992;33:325–329.
3. Messa C, Choi Y, Hoh CK, et al. Quantification of glucose utilization in liver metastases: parametric imaging of FDG uptake with PET. *J Comput Assist Tomogr* 1992;16:684–689.
4. Wahl RL, Cody RL, Hutchins GD, and Mudgett EE. Primary and metastatic breast carcinoma: initial clinical evaluation with PET with the radiolabeled glucose analogue 2-[^{18}F]-fluoro-2-deoxy-D-glucose. *Radiology* 1991;179:765–770.
5. Hawkins RA, Hoh CK, Dahlbom M, et al. PET Cancer Evaluations with FDG [Editorial]. *J Nucl Med* 1991;32:1555–1558.
6. Bares R, Altehoefer C, Cremerius U, et al. FDG-PET for metabolic classification of residual lymphoma masses after chemotherapy [Abstract]. *J Nucl Med* 1994;35:131P.
7. Phelps ME, Huang SC, Hoffman EJ, Selin CJ, Sokoloff L, Kuhl DE. Tomographic measurement of local cerebral glucose metabolic rate in humans with [^{18}]-fluoro-2-deoxy-D-glucose: validation of method. *Ann Neurol* 1979;6:371–388.
8. Huang SC, Phelps ME, Hoffman EJ, Sideris K, Selin CJ, Kuhl DE. Noninvasive determination of local cerebral metabolic rate of glucose in man. *Am J Physiol* 1980;238:E69–E82.
9. Patlak CS, Blasberg RG, Fenstenmacher JD. Graphical evaluation of blood-to-brain transfer constants from multiple-time uptake data. *J Cereb Blood Flow Metab* 1983;3:1–7.
10. Hawkins RA, Choi Y, Huang SC, Messa C, Hoh CK, Phelps ME. Quantitating tumor glucose metabolism with FDG and PET [Editorial]. *J Nucl Med* 1992;33:339–344.
11. Herholz K, Patlak CS. The influence of tissue heterogeneity on results of fitting nonlinear model equations to regional tracer uptake curves: with an application to compartmental models used in positron emission tomography. *J Cereb Blood Flow Metab* 1987;7:214–229.
12. Kubota R, Yamada S, Kubota K, Ishiwata K, Tamahashi N, Ido T. Intratumoral distribution of fluorine-18-fluorodeoxyglucose in vivo: high accumulation in macrophages and granulation tissues studied by microautoradiography. *J Nucl Med* 1992;33:1972–1980.
13. Hoffman FJ, Huang SC, Phelps ME. Quantitation in positron emission computed tomography: I. Effect of object size. *J Comput Assist Tomogr* 1979;3:299–308.
14. Zasadny KR, Wahl RL. Fit-constrained ("tumor-tailored") parametric images of cancer using FDG [Abstract]. *J Nucl Med* 1993;34:41P.
15. Choi Y, Hawkins RA, Huang SC, et al. Parametric images of myocardial metabolic rate of glucose generated from dynamic cardiac PET 2-[^{18}F]fluoro-2-deoxy-D-glucose studies. *J Nucl Med* 1991;32:733–738.
16. Kim CK, Gupta N, Chandramouli B, Alavi A. Standardized uptake values of FDG corrected for the body surface area are less dependent on the body size than SUVs corrected for the body weight [Abstract]. *J Nucl Med* 1993;34:73P.
17. Gupta NC, Chandramouli B, Frank A, Dewan N, Scott W. PET-FDG imaging for estimating probability of malignancy in solitary pulmonary nodules [Abstract]. *Radiology* 1993;147(suppl):189P.
18. Hamberg LM, Hunter GJ, Alpert NM, Choi NC, Babich JW, Fischman AJ. The dose uptake ratio as an index of glucose metabolism: useful parameter or oversimplification? *J Nucl Med* 1994;35:1308–1312.

Noninvasive Quantification of Dopamine D2 Receptors with Iodine-123-IBF SPECT

Masanori Ichise, James R. Ballinger, Haim Golan, Douglass Vines, Angela Luong, Scott Tsai and Hank F. Kung

Department of Nuclear Medicine, Mount Sinai Hospital, Department of Nuclear Medicine, Princess Margaret Hospital, University of Toronto, Toronto, Ontario Canada; and Division of Nuclear Medicine and Department of Radiology, University of Pennsylvania, Philadelphia, Pennsylvania

Iodine-123-iodobenzofuran (IBF) is a potent dopamine D2 receptor ligand suited for quantitative receptor studies. The purpose of this study was to evaluate three noninvasive methods of estimating the receptor parameter k_3/k_4 in humans with IBF-SPECT. **Methods:** Scans were acquired every 5 min for 180 min using a triple-headed SPECT system following a bolus injection of IBF (296 ± 37 MBq) in 14 normal volunteers. k_3/k_4 was estimated by the peak equilibrium ratio (R_{PE}) method and two proposed methods: a variation of the graphic method that derives the ratio of ligand distribution volumes (R_V) and area ratio (R_A) method, in which the ratio is calculated from the areas under the specific binding and nondisplaceable activity curves. **Results:** The mean R_{PE}, R_V and R_A were 2.74 ± 0.40, 3.06 ± 0.42 and 2.26 ± 0.28, respectively. Both R_{PE} and R_A underestimated R_V. The relationship between R_{PE} or R_A and R_V was linear ($p \leq 10^{-5}$. R_A showed higher correlation ($r = 0.94$) with R_V than did R_{PE} ($r = 0.90$). Simulations based on a tracer kinetic model showed that R_V, unlike R_{PE} or R_A, is affected by neither regional cerebral blood flow (rCBF) nor peripheral clearance rate (CR) of IBF. All three measures showed a significant decline with increasing age ($r = 0.54–0.58$, $p < 0.05$). **Conclusion:** R_V is preferred because it provides a theoretically valid estimate of k_3/k_4, independently of rCBF or CR. Alternatively, R_A might be preferred to R_{PE} because the former is simpler than the latter to implement yet the former provides a measure that equally well correlates with k_3/k_4.

Key Words: iodine-123-IBF; dopamine D2 receptors; brain SPECT; noninvasive quantification

J Nucl Med 1996; 37:513–520

The clinical usefulness of dopamine D2 receptor imaging using SPECT and [^{123}I]iodobenzamide (IBZM) (*1*) has been recently evaluated in several neuropsychiatric conditions (*2–9*). The more recently introduced [^{123}I]iodobenzofuran (IBF) (*10*) binds reversibly to D2 receptors with significantly higher affinity (K_D = 0.11 n*M*) and slightly lower lipophilicity compared with IBZM (*11*), provides higher image contrast and is suited for quantitative receptor studies (*12–14*).

For SPECT imaging of D2 receptors to be widely used, readily accessible yet valid methods to obtain quantitative information about the receptor are needed. In their recent IBF-SPECT study, Laruelle et al. (*14*) were able to measure the binding potential ($BP = B_{max}/K_D$) by using either kinetic or graphic analysis models. These methods, however, are not only invasive, requiring repeated arterial blood sampling, but also are technically demanding, requiring accurate measurements of both tissue and metabolite-corrected plasma concentrations as well as accurate cross-calibrations between the two types of measurements. Furthermore, there were marked individual differences in the rate of both peripheral metabolism and clearance of IBF with unmetabolized, free IBF representing only a small fraction in arterial plasma, and errors in the measurement of this fraction might have a significant effect on the binding potential estimation. Hence, they proposed alternatively to measure the receptor parameter k_3/k_4, the ratio of the transfer constants between the intracerebral nondisplaceable and specifically bound receptor compartments because this measure is independent of the free fraction of IBF.

On the other hand, the traditionally used empirical ratio method does not require blood sampling. Its outcome measure is obtained by calculating a basal ganglia-to-frontal cortex or

Received Jan. 12, 1995; revision accepted Jul. 5, 1995.

For correspondence or reprints contact: Masanori Ichise, MD, FRCP(C), Room 635, Nuclear Medicine, Department of Medical Imaging, Mount Sinai Hospital, 600 University Ave., Toronto, Ontario, Canada M5G 1X5.